

## THE HYDROGEN EPOCH OF REIONIZATION ARRAY DISH I: BEAM PATTERN MEASUREMENTS AND SCIENCE IMPLICATIONS

ABRAHAM R. NEBEN<sup>1</sup>, AARON EWALL-WICE<sup>1</sup>, NIPANJANA PATRA<sup>2</sup>, NITHYANANDAN THYAGARAJAN<sup>3</sup>, JAMES E. AGUIRRE<sup>4</sup>, ZAKI S. ALI<sup>2</sup>, JUDD BOWMAN<sup>3</sup> CARINA CHENG<sup>2</sup>, DAVID R. DEBOER<sup>2</sup> JACQUELINE N. HEWITT<sup>2</sup>, AARON PARSONS<sup>2</sup>

<sup>1</sup>MIT Kavli Institute, Massachusetts Institute of Technology, Cambridge, MA, 02139 USA

<sup>2</sup>Dept. of Astronomy, University of California, Berkeley, CA, USA

<sup>3</sup>Arizona State University, School of Earth and Space Exploration, Tempe, AZ 85287, USA and

<sup>4</sup>Dept. of Physics and Astronomy, University of Pennsylvania, Philadelphia, PA

*Draft version December 25, 2015*

### ABSTRACT

THIS WILL NEED TO BE REWRITTEN We deploy the 137 MHz ORBCOMM beam mapping system of Neben et al. (2015a) at the site of the HERA prototype at NRAO–Green Bank. This technique measures the beam of an antenna-under-test relative to that of a well-modeled reference antenna. We characterize environmental systematics such as reflections and multipath effects by comparing the measured beams of different reference antennas, then measure the beam pattern of the east-most HERA dish as a function of feed height over the dish surface. With the feed at the nominal focus of 4.5 m over the dish surface, the collecting area is observed to be 68.5 m<sup>2</sup>, agreeing with simulations. We also simulate delay spectra on baselines of different lengths and orientations at different LSTs for measured and model beams, and quantify the severity of and uncertainties in the delay space horizon brightening termed the “pitchfork effect” by Thyagarajan et al. (2015a). Future measurements will study the dish beam in the presence of adjacent dishes, quantifying levels of cross-talk and cross-coupling.

*Subject headings:* instrumentation: interferometers — techniques: interferometric — cosmology: observations — dark ages, reionization, first stars

### 1. INTRODUCTION

A new generation of low frequency radio telescopes is coming online with the goal of probing redshifted 21 cm emission from the Cosmic Dawn. These observations will complement indirect probes of the Dark Ages and Epoch of Reionization such as quasar sightlines, deep galaxy surveys, and the CMB optical depth which leave the reionization history of the universe only loosely constrained. (See Furlanetto et al. (2006); Morales & Wyithe (2010); Pritchard & Loeb (2012); Loeb & Furlanetto (2013); Zaroubi (2013) for reviews) Sensitivity and foreground removal are the main challenges in 21 cm observations, as the expected cosmological signal is 4–5 orders of magnitude fainter than Galactic and extragalactic foregrounds. Radio interferometers such as the Murchison Widefield Array (MWA) (Tingay et al. 2013; Bowman et al. 2013), the Precision Array for Probing the Epoch of Reionization (PAPER) (Ali et al. 2015b), the Giant Meterwave Radio Telescope (GMRT) (Paciga et al. 2011), and the Low Frequency Array (LOFAR) (van Haarlem et al. 2013) are seeking a first detection of cosmological 21 cm emission in power spectrum measurements, where the smooth frequency evolution of the foreground emission separates from the spectrally umsmooth cosmological signal whose frequency dimension probes the a line of sight through the inhomogenous reionizing universe.

The Hydrogen Epoch of Reionization Array (HERA) (Pober et al. 2014, , deBoer et al., submitted) is drawing on lessons learned by the MWA and PAPER to reach the calibration and foreground isolation accuracy required to make a significant detection and characterization of the cosmological signal. HERA uses 14 m diameter parabolic dishes arranged in a compact, hexagonal array to achieve

coherent integration on the very low surface brightness 21 cm signal. Redundant baselines also permit redundant calibration techniques which solve for internal degrees of freedom with only of parameters which must be estimated from the sky (Zheng et al. 2014), circumventing the sky model based calibration schemes which non-redundant arrays must pursue. HERA is pursuing a staged deployment of 19, 127, and finally 331 elements in progressively larger hex patterns, with scattered outriggers for imaging. A central lesson of first generation instruments is it is essential to characterize the instrument response to foreground emission lest instrument frequency dependence smear foreground power into cosmological signal modes.

It was initially thought that the foreground emission would be confined to the lowest few line of sight Fourier modes (e.g., Morales et al. 2006), however it was later realized that the interferometer’s frequency-dependent point spread function smears foreground power into a “wedge” shaped region in  $(k_{\perp}, k_{\parallel})$  Fourier space (Datta et al. 2010; Dillon et al. 2014; Pober et al. 2013; Morales et al. 2012; Vedantham et al. 2012; Thyagarajan et al. 2013; Trott et al. 2012; Liu et al. 2014a,b). This effect is straightforward to understand for a single baseline which measures the sky intensity weighted by the complex sky fringe  $e^{i\vec{k}\cdot\vec{b}}$ , where  $\vec{k} = \vec{k}(\theta, \phi, f)$  is the wave vector of the incident radiation,  $\vec{b}$  is the baseline vector in meters, and  $f$  is the observation frequency. Thus sources at different positions relative to the baseline vector manifest different frequency structure despite their intrinsically smooth spectra, but are geometrically limited by the baseline length to a maximum frequency dependence of  $e^{2\pi ifb/c}$ . This limits the foreground contamination to

a wedge shaped region in Fourier space with  $k_{\parallel} < ak_{\perp}$ , where  $k_{\perp}$  and  $k_{\parallel}$  represent spatial modes perpendicular and parallel to the line of sight, and  $a$  is a constant depending on the observational frequency and cosmology. The complement of the wedge is known as the “EOR window”.

It is convenient to phrase this description in terms of the delay in radiation arrival at the baseline’s two antennas,  $\tau$ , where  $\tau_{\max} = b/c$ . Sources at low delay have little frequency structure, while those near  $\tau = \tau_{\max}$  acquire the maximum frequency structure given the baseline length.

The fact that sources acquire frequency dependence based on their position on the sky tells us already that the primary beam strongly affects the aggregate frequency dependence of the foregrounds. The high delay regions of the sky lie near the horizon while low delay regions lie closer to zenith and also perpendicular to the baseline vector. Thyagarajan et al. (2015a) simulate the foreground contamination seen with a dipole beam, a phased array, and an Airy dish, and find that the latter suffers the least foreground leakage into  $k_{\parallel} > 0$  modes due to its narrow main lobe and minimal sidelobe levels. To be sure, all are subject to the same geometric limits on foreground frequency-dependence limiting foreground bounding foreground emission within the wedge, but the emission from high delay is better suppressed using the Airy dish leaving much of the wedge effectively empty.

So long as foreground emission is perfectly contained in the wedge it is irrelevant how much or little of it there is, but the finite bandwidth and imperfect bandpass calibration of real instruments smear power beyond the geometrical edge of the wedge into the EOR window. Sources at higher delay appear closest to the edge of the wedge, and thus are most at risk of leaking into the EOR window due to these effects. In fact, Thyagarajan et al. (2015a); Thyagarajan et al. (2015b) observe in simulations and then in data that while naively we might expect minimal emission at the very edge of the wedge because typical near-horizon beam responses are so small, two effects can cause a relative brightening of emission at those maximal delays, creating a characteristic “pitchfork” shape. This horizon brightening is caused by the large solid angle subtended by the near-horizon regions of the sky, as well as the apparent shortening of baselines when viewed nearly on axis at these elevations. This second effect makes intermediate length baselines of tens to hundreds of meters sensitive to the very bright diffuse emission would not see from near zenith. Together, these effects can overcome the decline in beam sensitivity near the horizon. All these considerations highlight the antenna beam as a critical design parameter for 21 cm observatories.

This is the first in a series of four papers detailing the HERA element. In this work we study angular response of the dish and its implications for power spectrum measurements. The three companion papers present reflectometry measurements (Patra et al., submitted) and simulations (Ewall-Wice et al., submitted) of the dish frequency response, as well as detailed foreground simulations for HERA (Thyagarajan et al., submitted). A general description to the design of the HERA experiment from an engineering point of view is given by DeBoer et al. (submitted). In essence, we require a large collecting area for sensitivity and minimal sidelobes and horizon

response without incurring the large cost per collecting area of very large dishes. A dish is preferred to a large phased array as it has fewer degrees of freedom and reduced potential of antenna-to-antenna variation (Neben et al 2015b, submitted). These factors naturally lead to a 14 m diameter parabolic dish with a dipole feed suspended at prime focus. The 352 dishes are positioned in a compact, hexagonal array permitting redundant baseline calibration and coherent integration in  $\vec{k}$  space (Zheng et al. 2014; Ali et al. 2015b).

In this paper we first characterize the angular response of a prototype HERA dish at the National Radio Astronomy Observatory–Green Bank. We use the beam mapping system of Neben et al. (2015a) to measure the 137 MHz beam pattern using the ORBCOMM satellite constellation. We obtain beam measurements out to zenith angles of  $\sim 60^{\circ}$  where the beam response is -35 dB relative to zenith, and compare with different numerical models. We characterize the dish beam at various feed heights to map out the focus and study beam errors due to feed misalignment. We compute the collecting areas and implied EOR power spectrum sensitivities of our measured beams. After verifying our numerical models, we consider the science implications of these beam patterns by foreground delay spectra at different baseline lengths and observing conditions to study when the horizon brightening effect is strongest, and thus, when foreground are most at risk of leaking into the EOR window.

In detail, we discuss the electromagnetic design and modeling of the dish in Section 2. We present the experimental setup of the beam mapping experiments and discuss their systematics, then review the ORBCOMM beam measurement system, in Section 3. We present our power pattern measurements in Section 4, and study the science implications of these beam measurements for foreground power spectra in Section 5, then conclude with discussion in Section 6.

## 2. DISH DESIGN AND MODELING

### NEEDS TLC

#### 2.1. Design of the HERA Dish

##### NEED EDITING

The 14 m HERA dish design is a departure from the large N-small D approach used by 21 cm observatories like PAPER and the MWA. Both observatories are actively pursuing power spectrum analyses using several year data runs, but the sheer data volume makes characterization and removal of systematics, as well as repeated or complimentary analyses, challenging. A larger element was chosen for HERA primarily to economize data volume. The natural consequence of a larger antenna aperture is a smaller field of view, but this is a small effect for 21 cm power spectrum analyses as our leverage on  $k$  modes in the spherically averaged power spectrum comes primarily from  $k_{\parallel}$  modes along the line of sight (in the frequency dimension).

However, such a turn from small, simpler antenna elements to larger, more complex dishes with suspended feeds must be done judiciously, lest the chromatic antenna response smear otherwise smooth spectrum foreground power into cosmological signal modes. For this

reason the dish design was carefully optimized for a foreground avoidance-based power spectrum spectrum analysis, as detailed by Parsons & DeBoer (2015) and discussed in the larger engineering context of HERA by DeBoer et al (in prep).



FIG. 1.— Aerial photograph of the two reference dipoles deployed in Galford Meadow at the National Radio Astronomy Observatory—Green Bank 100 m south of the HERA dish.



FIG. 2.— Aerial photograph of the two reference dipoles deployed in Galford Meadow at the National Radio Astronomy Observatory—Green Bank 100 m south of the HERA dish.

We summarize here the logic leading to a 14 m dish with  $f/D \approx 0.32$ . As discussed above, it is useful to think in delay-space, where a source ideally appears as a delta function at the delay corresponding to the difference in light travel time to two antennas in a baseline. In a real instrument, finite bandwidth and intrinsic source spectral structure (synchrotron sources typically have  $I \propto f^{-0.85}$ ) smear foreground power over a kernel as wide as  $\sim 60$  ns. All antennas have some frequency structure as well, though dipole-like elements such as sleeved dipoles and bowties may be made relative frequency independent over wide bands. Suspension of a feed over a dish introduces frequency structure directly due to time domain reflections between the dish and feed. We opti-

mize the HERA dish so this frequency structure extends no farther into delay space than the 60 ns intrinsic width of foregrounds. This was accomplished first through numerical modeling of the beam pattern with a PAPER dipole suspended over the dish aperture, and resulted in a maximum efficiency of 73% with  $f/d \approx 0.32$ . From there, using realistic estimates of reflection loss, a 14 m dish was observed to have the property that the signal received at the feed after two bounces (round trips between the dish and feed) is above -60 dB but contained in the wedge, but all higher order reflections in the EOR window are below -60 dB, and thus an order of magnitude smaller than the expected cosmological signal.

In reality, the HERA dishes are somewhat more complicated than these simple considerations imply, and part of the purpose of the beam measurements presented in this paper is to characterize their *in situ* beam patterns. The dish is fabricated out of low cost construction materials with an expected lifetime of  $\sim 5$  years, sufficient to detect the 21 cm power spectrum to high significance before the Square Kilometer Array builds a longer lasting instrument to more fully characterize the Epoch of Reionization with imaging. The feed consists of a sleeved dipole, suspended in a cage structure from three ropes attaching to telephone poles spaced around the dish. The dipole is mounted on a XX m mast over a XX m diameter backplane surrounded by a XX m long cylindrical “skirt” designed to reduce cross coupling with adjacent elements by narrowing the feed’s response. The dish surface consists of 12 wire mesh strips secured to 60 mm PVC pipes forming the dish skeleton. A spar at 2.4 m elevation is added to ensure approximately parabolic shape. Note that we refer to this design as a *faceted parabola* given that the dish surface between PVC spars is not curved, though our design ensures the Ruze loss is at the percent level. A door is engineered into one of these mesh strips to facilitate feed maintenance.

This work presents beam pattern measurements to verify the capabilities of this new dish, in particular the position of the dish focus, the shape of the main lobe, the magnitude of the dish sidelobes, the degree of beam symmetry, the actual dish/feed efficiency (i.e., collecting area), and the expected level of antenna-to-antenna variation.

## 2.2. Dish Modeling

ASK DAVE OR RICH TO WRITE A ONE OR TWO PARAGRAPH SUMMARY OF THE ELECTROMAGNETIC DISH SIMULATIONS

## 3. EXPERIMENTAL SETUP

### 3.1. ORBCOMM Beam Mapping System Review

We briefly review the beam mapping system detailed by Neben et al. (2015a), then discuss application of system for HERA dish measurements. The system takes advantage of the 137 MHz communications satellites operated by ORBCOMM Inc. as bright point sources which, by virtue of their number ( $\sim 30$ ), short orbital periods ( $\sim 90$  minutes), and orbital precession cover  $\sim 65\%$  of the visible sky in just a few days. The coverage from the Green Bank site is limited by the fact that the satellites’ orbital inclinations are all less than  $45^\circ$ .

Unlike celestial source beam measurements, where the flux may be assumed constant over the timescale of the

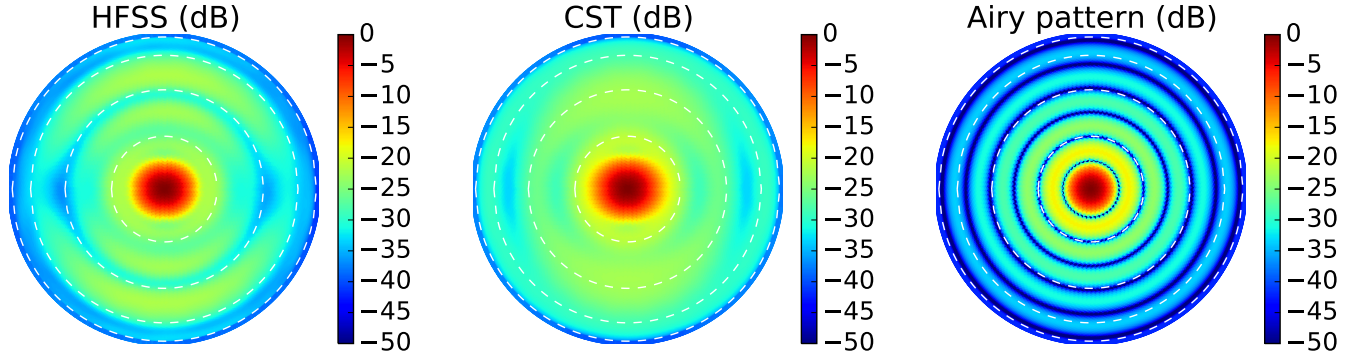


FIG. 3.— Simulated delay spectra for the GSM and point sources at  $0^\circ$  (top pair) and  $60^\circ$  (bottom pair) LST for EW baselines of length 14 m (left pair) and 42 m (right pair). The beams are assumed constant over frequency.

measurement, satellite fluxes can vary rapidly due to changing distance, orientation, and transmission power. To correct for this, we measure the satellite flux in each ground polarization (EW and NS) using a simple, well-modeled reference antenna. Comparison of this measured power with that observed in the Antenna-Under-Test (AUT) gives the AUT beam response in the direction of the satellite. An equivalent interpretation of the measurement is that the power ratio between the AUT and the reference antenna gives the relative beam response in the satellite direction, and multiplication by the reference antenna model yields the desired AUT response. As discussed in Neben et al. (2015a), this procedure correctly measures the response of the AUT to unpolarized radiation despite the fact that satellite signals are generally polarized.

In detail, we measure the dual-polarization RMS power received by each antenna in 512 2 kHz channels across the 137–138 MHz band. Each band power is averaged over  $\sim 0.2$  sec. There are 0–3 satellites above the horizon at any given time transmitting on different  $\sim 15$  kHz wide sub-bands in 137–138 MHz. By observing at many different frequencies, we probe the beam response in all these directions simultaneously. We compute the satellite positions using the orbital elements published by Celestrak<sup>1</sup> and the orbital integrator predict<sup>2</sup>. However, the satellite frequencies vary occasionally to avoid interference within the constellation. Zheng et al. (2014) use interferometric phases to identify and exclude times when multiple satellites are in view. As our data acquisition system makes only total power measurements, we instead use an ORBCOMM interface box (typically supplied to commercial users of the network) to sync with passing satellites and record their identifier and transmission frequency during each pass.

In this way, beam measurements are built up along satellite tracks over the course of several days of integration, yielding typically 200–300 satellite pass. Each pass is processed separately to identify and exclude times of low signal-to-background when the satellite is low in the sky or in the off state of a pulsing sequence. At those times, then satellite flux no longer dominates over that of the diffuse Galactic background, and a power measurement no longer probes the response in only the satellite direction. The beam measurements are then gridded in

horizontal coordinates in HEALPix (Górski et al. 2005) with a resolution of  $1.8^\circ$  ( $n_{\text{side}}=32$ ). As a last quality control step to reject errant beam measurements due to RFI, for instance, we keep only the central 90% of  $\sim 50$  measured beam values in each HEALPix cell.

### 3.2. HERA–Green Bank: A three-element prototype array

A 3-element HERA engineering prototype is being constructed at the National Radio Astronomy Observatory–Green Bank. We performed the beam measurements presented in this work on the first of these dishes to be constructed, future work will characterize its beam in the presence of the other two dishes once they are constructed. The prototype array is situated in Galford Meadow, approximately 1 km southwest of the Green Bank Telescope. Note that unlike the full HERA site in the Karoo Desert Radio Astronomy Reserve in South Africa, the Green Bank site has trees and foothills, as well as moist ground. Our beam measurements are sensitive to these effects in addition to the construction imperfections of real world dishes.

We use a simple dual-polarization dipole as our reference antenna. The dipole is constructed out of copper tubing covered by PVC for protection, mounted above a  $2 \text{ m} \times 2 \text{ m}$  ground plane. See Neben et al. (2015a) for details. During the dish measurements the dipole is positioned 100 m due south of the dish, though we experiment with other locations at first in our to characterize the environmental systematics of these measurements, as detailed in the next section.

### 3.3. Assessing Experimental Systematics

As in Neben et al. (2015a), we assess systematics using a “null experiment” in which we use a second reference dipole as the antenna-under-test (AUT). Taking the ratio of its measured power pattern with the model beam pattern amounts to a ratio of the raw power responses received by the two antennas as a function of satellite direction. This probes the level of environmental systematics (i.e., reflections and varying ground properties) and antenna fabrication imperfections which affect each antenna differently. This is not a probe of modeling imperfections common to both antennas, but we expect such errors to be subdominant as the physical properties of the antenna are easier to characterize, and thus simulate, than misalignments and local environmental effects.

<sup>1</sup> <http://www.celestrak.com/NORAD/elements/orbcomm.txt>

<sup>2</sup> <http://www.qsl.net/kd2bd/predict.html>

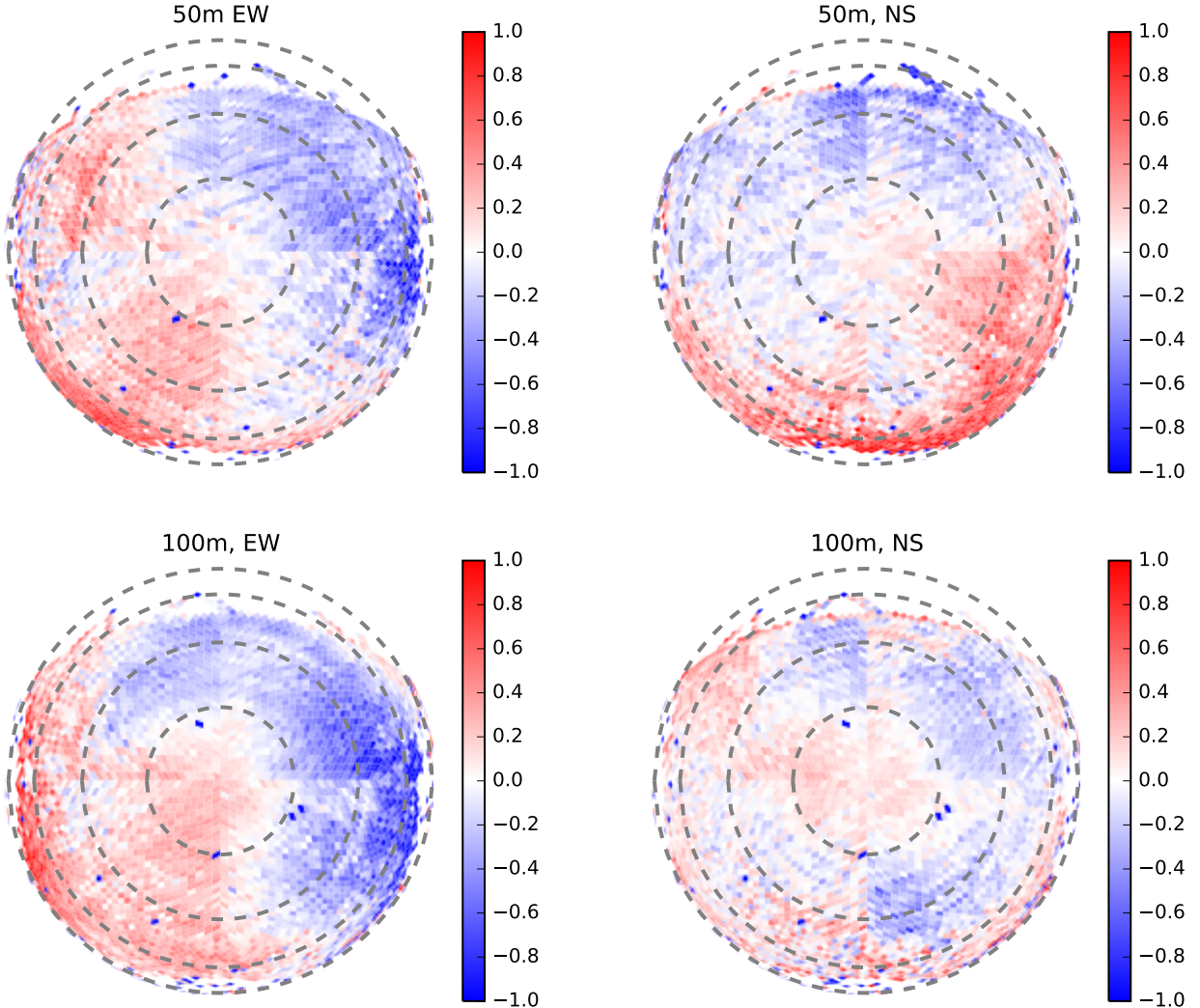


FIG. 4.— We characterize the accuracy of the beam measurement system through null experiments in which a second reference antenna is taken as the AUT and ratio of both reference antenna power patterns is measured for EW (left) and NS (right) polarizations. The reference antennas are separated by 50 m from each other and from the HERA dish in the first experiment (top), and by 100 m from each other and from the HERA dish in the second experiment (bottom).

As we are not able to replace the HERA dish with a reference antenna, we run two null experiments with both reference dipoles deployed (1) 50 m apart on a NS line, 50 m south of the HERA dish; and (2) 100 m apart on a NS line, 100 m south of the HERA dish. Figure ?? shows the results from these experiments in the form of the ratio of the power responses of the two antennas. We collected roughly 100 satellite passes. Systematics at the few percent level are observed in within  $20^\circ$  of zenith, and at the  $10 - 20\%$  level farther out. The magnitude and angular distribution of these systematics changes modestly as the separation is changed, suggesting that the reference dipoles differ largely due to intrinsic differences, with some environmental variation. In any case, these fractional errors propagate directly into our measured dish power patterns.

#### 4. DISH MEASUREMENTS

##### 4.1. Power pattern measurements

We make three dish power pattern measurements with the feed at different heights: (1) 4.5 m, the nominal dish focus; (2) 5.0 m, an intermediate focus; and (3) 5.3 m, the numerically determined focus of the dish/feed system, where all heights are measured from the dish surface to the feed back plane. In each configuration we collect data for 2–4 days, obtaining roughly 200 satellite passes. We exclude times when the received power is within 20 dB of the background level determined at between passes, and then grid measured beam values into  $1.8^\circ$  HEALPix cells on the sky, rejecting outliers in the top or bottom 5% in each cell as a final guard against rare satellite identification problems or ADC saturation issues.

Figure 5 shows the measured power patterns for these three feed heights for the EW (left panel) and the NS (right panel) feed polarization. These maps are plotted in sine-projection with dashed circles marking zenith angles of  $20^\circ, 40^\circ, 60^\circ, 80^\circ$ . The sky coverage in these dish measurements extends out to typically  $\theta \sim 50 - 60^\circ$ . Beyond that the ORBCOMM flux is sufficiently attenuated relative to diffuse galactic emission that a power ratio measurement between the two antennas is no longer a clean probe of their gains in the direction of the satellite. At these zenith angles, the beam sidelobes are roughly -30 dB, and are trending downward at the edge of the measured region.

The roughly  $10^\circ$  main lobe narrows slightly as the feed is raised from 4.5 m to 5.3 m, and the sidelobes shrink both in size and in amplitude, confirming the numerically predicted focus of 5.3 m. As expected, the EW main lobes are slightly wider in the NS direction. In theory, the only asymmetric part of the dish is the dipole feed, so the overall beam should have a  $180^\circ$  azimuthal symmetry. We observe deviations from this symmetry at the few dB level in the sidelobes, suggesting dish surface and/or feed imperfections given that the systematics identified in the null experiment are smaller.

Figure 6 shows slices through the E and H planes of these power patterns along with the HFSS and CST numerical models discussed earlier. As in the previous plot, the EW and NS beams are shown in the left and right panels, while the different feed heights are shown in the different rows. The data agree with both models to within a dB in the main lobe, but begin to diverge

in the sidelobes at zenith angles of  $20^\circ$  and larger. Here the evolution of the sidelobes as the feed is raised is again seen starkly, as is the fact that the main lobes are slightly wider along the H planes than along the E planes.

##### 4.2. Sensitivity

We compute the effective collecting areas of these beam patterns by first interpolating over unmeasured cells and smoothly extrapolating the power pattern to the horizon. These operations produce a realistically smooth beam which reaches roughly -30 dB at the horizon, as suggested by the numerical models. The collecting area is related to the power pattern as

$$A = \frac{\lambda^2 B(0,0)}{\int B(\theta, \phi) d\Omega} \quad (1)$$

The collecting areas range are shown in Table 1 along with the maximal collecting area achieved by the Airy pattern for a 14 m dish. The measured collecting areas are a 30–50% lower than the geometric area. This is in line with expectations given that the Airy pattern has the largest possible collecting area, equal to the dish cross section, and the feed’s backplane and cylindrical skirt reduce it. However we opt for this reduction over added collecting area in order to reduces the azimuthal beam asymmetry and minimize the cross-coupling between adjacent dishes.

TABLE 1  
COLLECTING AREA ( $m^2$ ) OF MEASURED 137 MHZ BEAMS AND CORRESPONDING POWER SPECTRUM SNR FOR HERA-127.

Beam	$A_{\text{eff}}$ ( $m^2$ )	SNR (pess, mod, opt)
Airy pattern	155	9.1, 11.0, 37.2
Measured, feed at 5.3 m	97.9	8.2, 8.3, 29.2
Measured, feed at 5 m	82.6	6.8, 6.9, 26.5
Measured, feed at 4.5 m	73.6	6.4, 6.5, 24.8

We run 21cmSense<sup>3</sup> to compute the overall SNR of a power spectrum detection with one season (6 hours per night for 180 nights) of HERA-127 data. To input these collecting areas into 21cmSense, we convert these measured dish collecting areas into effective dish diameters, which we input as the `dish_size_in_lambda` parameter. We predict the SNRs with optimistic, moderate, and pessimistic foreground assumptions. In the optimistic case,  $k$  modes inside the same  $uv$  pixel are added coherently, and all modes whose frequency dependence is larger than that of source at the edge of the main lobe are used. In the moderate case,  $k$  modes inside the same  $uv$  pixel are added coherently and only modes whose frequency dependence falls outside of the horizon plus a buffer are used. In the pessimistic case, all baselines are added incoherently and only modes outside the horizon plus a buffer are used.

The SNRs computed with the measured collecting areas fall from 9–11 for the Airy pattern to 6–8 in the pessimistic and moderate cases. In the optimistic case, the SNR falls from 37 with the Airy pattern to 24–29 with the measured collecting areas. In all cases this reduction is a loss of sensitivity, but a power spectrum detection is still always very significant at the  $6\sigma$  level or better.

<sup>3</sup> <https://github.com/jpober/21cmSense>

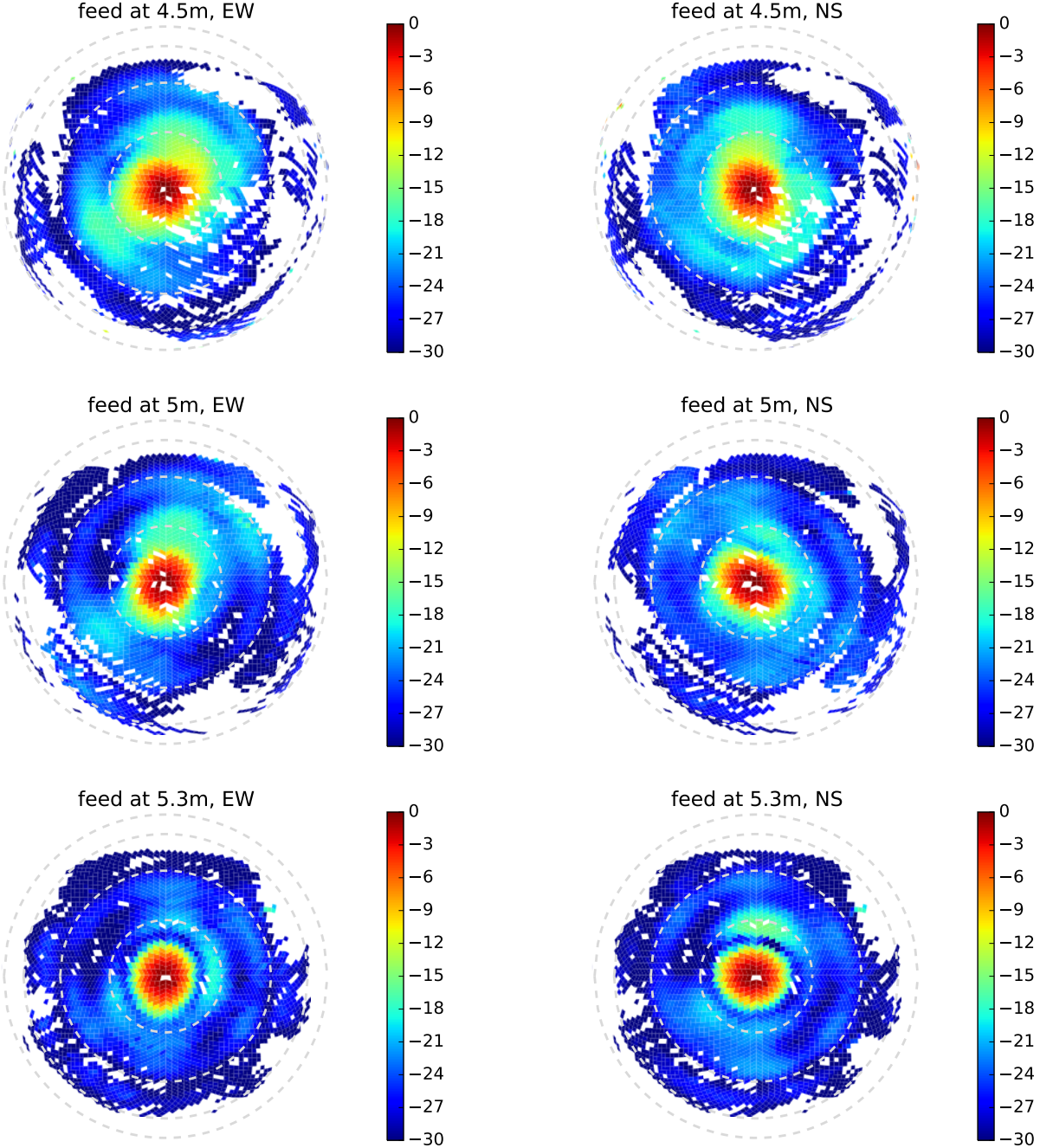


FIG. 5.— null experiment beam ratio plots

##### 5. FOREGROUND DELAY SPECTRA SIMULATIONS

We turn in this section to the effects of the beam power pattern on the apparent frequency dependence of the foregrounds. Thyagarajan et al., (submitted) discuss the apparent frequency dependence of foregrounds in more detail as well as methods to mitigate it such as delay space CLEANing. We focus on this section on the uncertainties in these foreground power spectrum simulations due to beam modeling uncertainties, but we must first discuss these foreground simulations themselves and their dependence on observing conditions.

We simulate foreground power spectra using differ-

ent primary beam models at various local sidereal times (LSTs). Given that our measured dish power patterns agree well with both numerical models (HFSS and CST) in the main lobe but deviate in the sidelobes, and that these models make somewhat different assumptions about the dish surface, we take them as a representative pair of possible dish models. We use a feed height of 5 m, a compromise between larger collecting area and smaller risk of coupling to adjacent dishes. We also include the Airy pattern for comparison as Thyagarajan et al. (2015a). Beam models with weaker response near the horizon (such as the Airy pattern) downweight sources in this direction of high apparent frequency dependence.

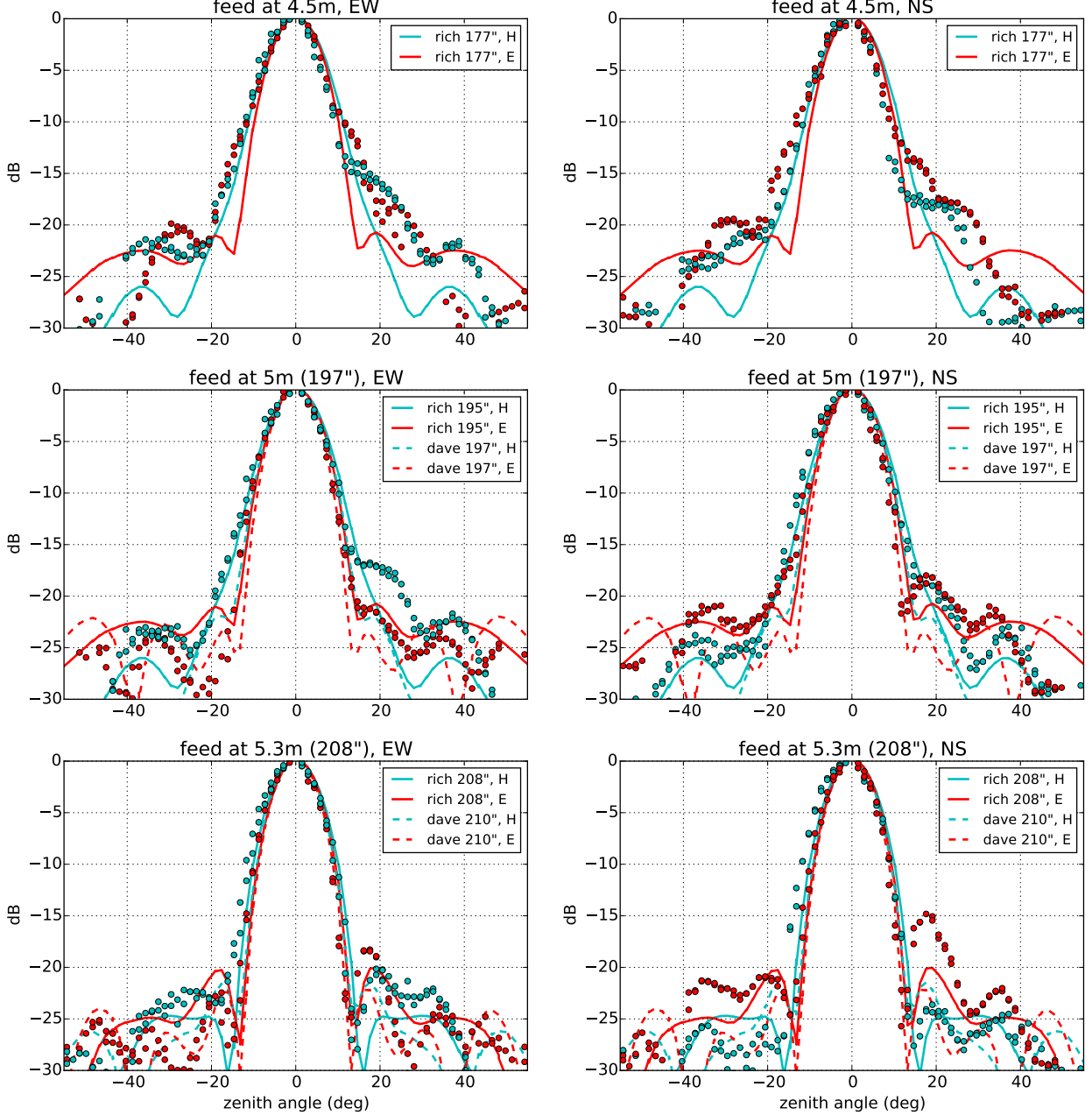


FIG. 6.— null experiment beam ratio plots

This reduces the magnitude of emission near the edge of the EOR window, reducing the risk it leaks inside. We use the per-baseline approach of Parsons et al. (2012b,a), simulating visibilities measured by specific baselines as a function of frequency, then computing the Fourier transform over frequency (delay transform) and normalizing the result into a cosmological power spectrum following Thyagarajan et al. (2015a).

In detail, we simulate visibilities for each beam model at various LSTs, modeling the sky as the sum of the Global Sky Model (de Oliveira-Costa et al. 2008) and the Culgoora (Slee 1995) and MWA Commissioning Survey (Hurley-Walker et al. 2014) point source catalogs. We use a frequency spacing of 1 MHz, sufficient to characterize delays within and just outside of the horizon limits on

both baseline lengths we are concerned with, 14 m and 42 m. We use a total bandwidth of 100 MHz (50 MHz after applying the Blackman-Harris window) centered on 150 MHz. This bandwidth is larger than the 10 MHz thought to be safe from signal evolution over redshift, but is the bandwidth used in the wide band delay space foreground CLEAN of Parsons et al. (2014); Ali et al. (2015a).

Figure 7 (top panel) shows simulated foreground delay spectra at various LSTs using the nominal HFSS beam. As all these LSTs are high galactic latitudes far from the galactic center, the total visibility power (the level of the zero delay mode) varies only by a factor of a few over these LSTs on both baseline lengths (14 m (left panel), 42 m (right panel)). However the negative delay horizon

limit (corresponding to the western horizon) has a peak that varies by over three orders of magnitude on the 14 m baseline and by two orders of magnitude on the 42 m baseline, demonstrating the stark difference in horizon brightening when the galaxy is just above versus just below the horizon.

In this figure we perform the approximate conversion from delay  $\tau$  to  $k_{\parallel}$ , which we plot as a second  $x$ -axis at the top of the plot. For these short baselines,  $k_{\parallel}$  may be converted to  $k$  by adding  $k_{\perp} = 0.005$  for the 14 m baseline or  $k_{\perp} = 0.02$  for the 42 m baseline in quadrature. These numbers are small compared to the range of  $k_{\parallel}$  plotted, and thus we interpret the  $k_{\parallel}$  axis as simply the  $k$  axis, and plot a 1D model power spectrum computed using 21cmFast (Mesinger et al. 2011) as a dotted line for comparison.

To characterize the effect of beam modeling uncertainties on this horizon brightening, we select two of these LSTs, one with maximal horizon brightening ( $2^{\circ}$ ), and one with minimal horizon brightening ( $62^{\circ}$ ). Figure 8 shows the sine-projected Global Sky Model, which dominates the horizon brightening effect, in horizontal coordinates with units of Kelvin for both LSTs. Dashed lines mark zenith angles  $20^{\circ}, 40^{\circ}, 60^{\circ}, 80^{\circ}$ . These plots confirm that the large negative delay peak at the  $2^{\circ}$  LST is due to the center of the galaxy just above the horizon. In contrast several hours later, the galactic center is fully below the western horizon, leaving only a slight brightening near the eastern horizon due to the weaker galactic anticenter.

How much do the predicted foreground power spectra differ between the three model dish power patterns? Figure 7 (middle panel) shows the simulated delay spectra for all three beams at  $2^{\circ}$  LST, when the horizon brightening is worst. All three delay spectra agree out to delays of 10–20 ns on the 14 m baseline and 30–40 ns on the 40 m baseline. These numbers suggest that the beams track each other fairly well out to  $15\text{--}20^{\circ}$  from zenith, beyond which they diverge. This is roughly what is observed in Figure 6 (middle panel). At larger delays, especially near the negative delay horizon limit, all three model delay spectra diverge due to the significant edge brightening which effectively discriminates between these models. The CST, HFSS, and Airy beams reach roughly -35 dB, -38 dB, and -50 dB at the horizon (Figure 3), consistent with the fact that the CST beam has the largest horizon brightening, followed by the HFSS beam, and then by the Airy beam. This is seen in the delay spectra for both baseline lengths, though the edge brightening is much clearer on the longer baseline where it less diluted by zero delay emission.

In contrast, all three model agree much more closely when there is little or no edge brightening as in Figure 6 (bottom panel) where we plot the delay spectra for all three beams for  $62^{\circ}$  LST. There is still a modest flattening off near the horizon on the 14 m baseline and a slight peak on the 42 m baseline due to the large solid angle near the horizon. However as the near horizon emission at this LST is roughly the same temperature as emission from everywhere else on the sky, the difference between the three beam models is greatly reduced.

## 6. DISCUSSION

NEEDS TLC

Power spectrum analyses by first generation 21 cm observatories are ongoing, but are contending with challenges ranging from calibration and foreground modeling to the computing time required to process thousands of hours of data. HERA draws the most successful ideas from these first generation instruments, pursuing a compact and redundant array layouts, large collecting area antenna elements, and per-baseline power spectrum analysis to make advances exactly where necessary to make a first detection and characterization of the 21 cm signal from the EOR. In pursuing an array of dishes rather than one of fixed dipoles, HERA turns away from the large  $N\text{-small } d$  approach used by the MWA, LOFAR, PAPER, and other first generation instruments in order to achieve sufficient sensitivity at a reasonably data processing and analysis cost. The papers in this series characterize the 14 m diameter dish used as HERA’s antenna element using reflectometry measurements and simulations which probe the beams gain variation with frequency, as well as beam pattern measurements and simulations which probe the beams angular variation.

We present in this paper beam pattern measurements at 137 MHz and comparisons with beam models, as well as simulations of the foreground delay spectra using these modeled beams. We adapt the beam mapping system of Neben et al. (2015a), deploying it at the prototype three-element HERA array at the National Radio Astronomy Observatory–Green Bank. Only one dish had been constructed when these measurement were made. We present measured power patterns for three different feed heights above the dish covering much of the visible sky probing down to -30 dB relative to the zenith response. The measured beams agree well with both models in the main lobe out to  $10\text{--}20^{\circ}$  from zenith, then roughly track the sidelobe levels at 20–30 dB below zenith, though fail to reproduce the exact sidelobe amplitudes and locations.

These deviations are larger than the  $\pm 1$  dB systematics observed in the null experiments designed to probe the accuracy of the ORBCOMM beam measurement system as deployed at this location, suggesting they are accurate measurement of the in situ beam pattern of the imperfect HERA dish. The most likely dish non-idealities are dish surface imperfections and feed misalignment, both of which may vary from antenna to antenna in the full HERA array. Characterizing this antenna-to-antenna beam variation and its effects on power spectrum analyses for HERA, in the way Neben et al (submitted) do for the MWA, is left as future work.

We quantify the 21 cm power spectrum sensitivity using our measured beam patterns by first computing the collecting area at different feed heights. We observe a reduction of 30–50% from that of an ideal, unobstructed Airy pattern for a 14 m dish. We convert these collecting areas into effective dish sizes to predict overall power spectrum sensitivities for HERA-127 using 21cmSense, and find SNRs of 6–8 in pessimistic and moderate foreground scenarios, and 24–29 in optimistic ones, to be compared with roughly 10 and 37 using the Airy dish. This is a certainly a reduction, but of course an unobstructed, perfectly azimuthally symmetric Airy pattern is unachievable, every dish required polarized feeds either placed on axis where they block the primary reflector, or placed off axis where they don’t get the dish’s full collect-

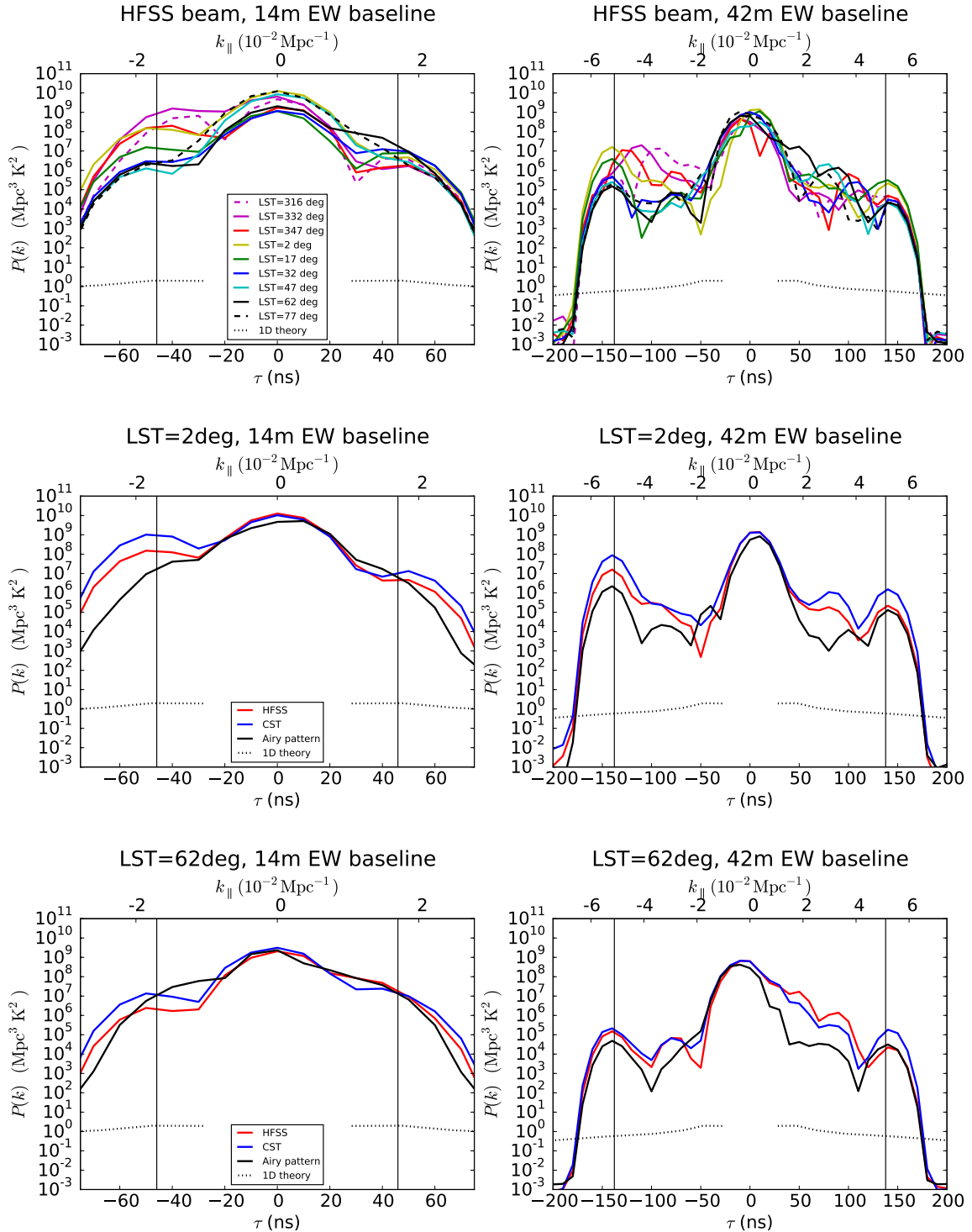


FIG. 7.— Simulated foreground delay spectra using the HFSS beam at various LSTs (top panel). We plot the delay spectra at two LSTs spanning the range of possible horizon brightening for three different beam models. The maximum horizon brightening at the negative horizon occurs at  $2^\circ$  LST (middle panel), and the three beam models thus differ markedly in their predicted delay spectra near the horizon. In contrast, when the horizon brightening effect is smaller at  $2^\circ$  LST, the foreground delay spectra from all three beams agree much more closely.

ing area. Further, the XX m cylinder hung from the feed backplane around the dipole mitigates cross-coupling between adjacent dishes and reduces azimuthal asymmetry, both of which facilitate analysis despite the reduced sensitivity.

Beyond simply sensitivity considerations, though, different beam models affect science analyses by reweighting celestial emission in different regions of the sky which are imprinted by the interferometer with different frequency dependence. Understanding this “wedge” region in cylindrical fourier space has proved a fruitful advance in 21 cm analyses over the past several years. Foregrounds acquire frequency dependence only from the changing baseline length in wavelengths with frequency, reaching a maximum fringe rate for a source at the horizon in line with the baseline. The complement of the wedge is the EOR window, which is where detection of the EOR signal is theoretically possible without foreground subtraction as it is nominally clear of foregrounds.

However Nithya has highlighted that distribution of foregrounds within the wedge is important as well. The beam response at low elevations determines whether there is a brightening at the geometric, horizon limit due to the increasing solid angle and a sufficiently shallow beam gradient at low elevations. This produces a characteristic “pitchfork” shape in the delay spectrum of a single baseline, with a zero delay peak due to near-zenith emission surrounded by tines at the negative and positive horizon limits due to emission from the two horizon directions in line with the baseline. These horizon peaks are most at risk of corrupting the outer modes of the

EOR window due to leakage from the delay point spread function.

We have simulated foreground delay spectra for different baseline lengths and LSTs, finding that the level of this horizon brightening is largest when the galaxy is just above the horizon, and lowest when it is well below. When this pitchfork effect is large, our uncertainty in it due to beam modeling uncertainty is also large, as evidenced by the deviation of our HFSS and CST numerical beam models for these simulations. When the effect is small, the two beam models produce much more similar results, highlighting the delay spectrum as an exquisite probe of the challenging to measure beam response at very low elevations.

As discussed by the other papers in this series, the frequency dependence of the beam power pattern and its overall gain widen the delay kernel of a source at some delay, leaking power farther into the EOR window. These papers demonstrate that in the best case, a combination of bandpass calibration and delay space CLEANing can mitigate foregrounds to a manageable level, while in the worst case, HERA can still achieve a XX–XX  $\sigma$  detection of the EOR parameters from the power spectrum by simply excluding a very conservative buffer at the edge of the EOR window. All these considerations highlight the need for precision characterization of antenna elements and their implications for 21 cm science analyses on the part of next generation observatories if we are to have any hope of detecting making this challenging measurement.

## REFERENCES

- Ali, Z. S., et al. 2015a, ApJ, 809, 61  
 —. 2015b, ArXiv e-prints  
 Bowman, J. D., et al. 2013, TrottObservingModes, 30  
 Datta, A., Bowman, J. D., & Carilli, C. L. 2010, ApJ, 724, 526  
 de Oliveira-Costa, A., Tegmark, M., Gaensler, B. M., Jonas, J., Landecker, T. L., & Reich, P. 2008, MNRAS, 388, 247  
 Dillon, J. S., et al. 2014, Phys. Rev. D, 89, 023002  
 Furlanetto, S., Oh, S., & Briggs, F. 2006, Physics Reports, 433, 181  
 Górski, K. M., Hivon, E., Banday, A. J., Wandelt, B. D., Hansen, F. K., Reinecke, M., & Bartelmann, M. 2005, The Astrophysical Journal, 622, 759  
 Hurley-Walker, N., et al. 2014, PASA, 31, 45  
 Liu, A., Parsons, A. R., & Trott, C. M. 2014a, Phys. Rev. D, 90, 023018  
 —. 2014b, Phys. Rev. D, 90, 023019  
 Loeb, A., & Furlanetto, S. R. 2013, *The First Galaxies In The Universe* (Princeton University Press, Princeton, NJ)  
 Mesinger, A., Furlanetto, S., & Cen, R. 2011, MNRAS, 411, 955  
 Morales, M. F., Bowman, J. D., & Hewitt, J. N. 2006, ApJ, 648, 767  
 Morales, M. F., Hazelton, B., Sullivan, I., & Beardsley, A. 2012, ApJ, 752, 137  
 Morales, M. F., & Wyithe, J. S. B. 2010, Annual Reviews of Astronomy and Astrophysics, 48, 127  
 Neben, A. R., et al. 2015a, Radio Science, 50, 614  
 Paciga, G., et al. 2011, Monthly Notices of the Royal Astronomical Society, 413, 1174  
 Parsons, A., Pober, J., McQuinn, M., Jacobs, D., & Aguirre, J. 2012a, ApJ, 753, 81  
 Parsons, A. R., & DeBoer, D. R. 2015, Configuration of the HERA Element, Tech. Rep. 5, HERA Memo Series  
 Parsons, A. R., Pober, J. C., Aguirre, J. E., Carilli, C. L., Jacobs, D. C., & Moore, D. F. 2012b, ApJ, 756, 165  
 Parsons, A. R., et al. 2014, ApJ, 788, 106  
 Pober, J. C., et al. 2013, ArXiv e-prints  
 Pober, J. C., et al. 2014, The Astrophysical Journal, 782, 66  
 Pritchard, J. R., & Loeb, A. 2012, Reports on Progress in Physics, 75, 086901  
 Slee, O. B. 1995, Australian Journal of Physics, 48, 143  
 Thyagarajan, N., et al. 2013, The Astrophysical Journal, 776, 6  
 —. 2015a, ApJ, 804, 14  
 Thyagarajan, N., et al. 2015b, ApJ, 807, L28  
 Tingay, S. J., et al. 2013, Publications of the Astronomical Society of Australia, 30  
 Trott, C. M., Wayth, R. B., & Tingay, S. J. 2012, ApJ, 757, 101  
 van Haarlem, M. P., et al. 2013, A&A, 556, A2  
 Vedantham, H., Udaya Shankar, N., & Subrahmanyan, R. 2012, ApJ, 745, 176  
 Zaroubi, S. 2013, in *Astrophysics and Space Science Library*, Vol. 396, *The First Galaxies*, ed. T. Wiklind, B. Mobasher, & V. Bromm (Springer Berlin Heidelberg), 45–101  
 Zheng, H., et al. 2014, Monthly Notices of the Royal Astronomical Society, 445, 1084  
 Zheng, H., et al. 2014, MNRAS, 445, 1084

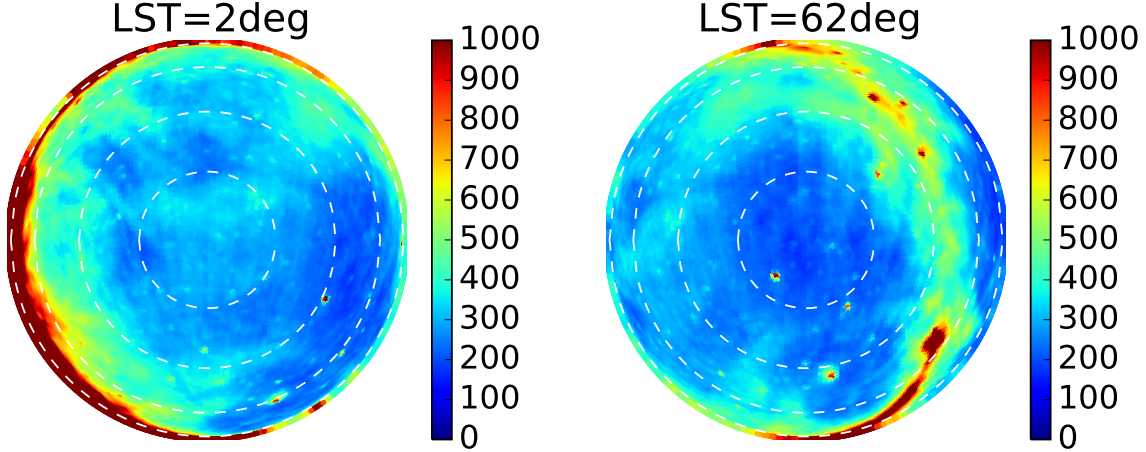


FIG. 8.— Global Sky Model (de Oliveira-Costa et al. 2008) in sine-projected horizontal coordinates at LST of  $2^\circ$  (left) and  $62^\circ$  right. The very bright emission from the center of the galaxy at the western horizon at  $2^\circ$  is seen in the delay spectra of EW baselines as a horizon brightening at negative delay.